

The metallicities of little red dot host galaxies: LRDs are metal poor, but not pristine

G. P. Nikopoulos[1,2,⋆], D. Watson[1,2,⋆⋆], C. L. Pollock[1,2], A. Sneppen[1,2], K. E. Heintz[1,2,3], J. Witstok[1,2], and G. Brammer[1,2]

[1] Cosmic Dawn Center (DAWN), Denmark
[2] Niels Bohr Institute, University of Copenhagen, Jagtvej 155A, DK-2200, Copenhagen N, Denmark
[3] Department of Astronomy, University of Geneva, Chemin Pegasi 51, 1290 Versoix, Switzerland

Received July XX, 2026

ABSTRACT

Context. Little Red Dots (LRDs) are a population of high-z sources discovered by *JWST* whose compactness, broad permitted lines, strong absorption features, continuum shapes and luminosities point to accreting supermassive black holes (SMBHs) embedded in dense gas. To date, the metallicity of the hosts of these systems has not been systematically measured.
Aims. We determine the gas-phase metallicities of LRD host galaxies and test whether their narrow-line emission is consistent with chemically pristine gas, metal poor star formation or AGN activity.
Methods. We assemble a sample of 24 LRDs at $z \approx 2.3$–7 with medium and high-resolution *JWST*/NIRSpec data. We derive oxygen abundances and electron temperatures using the direct T_e method applied exclusively to the narrow components of emission lines, and cross-check against widely used strong line calibrations.
Results. We derive a sample-averaged abundance of $Z_{T_e} = 0.08^{+0.11}_{-0.03}\,Z_\odot$ ($T_e = 23000^{+17000}_{-7000}$ K), placing LRDs firmly in the metal-poor regime of high redshift star forming galaxies. The $\hat{R}$ calibration yields a consistent average of $Z_{\hat{R}} = 0.07^{+0.07}_{-0.04}\,Z_\odot$, with only 4% scatter relative to the direct T_e method, providing a robust proxy for systems where the [O III] 4363 Å line is not detected. Using the strong-line method, we identify two extremely metal-poor LRDs with metallicities <1.3%.
Conclusions. The general population of LRDs are among the lower metallicity galaxies found by *JWST* at this epoch and are an order of magnitude below metallicities of typical Seyfert or quasar host galaxies. They exhibit a narrow range of metallicities with a range of about 0.6 dex, which remains remarkably stable over cosmic time. Such low metallicity may then be a defining property of the class. The fact that LRDs have substantial metallicity across most of the class poses a challenge to models that require formation via pristine gas collapse, while their generally low metallicity indicates that they are not standard AGN.

Key words. Galaxies: abundances – Galaxies: active – Galaxies: high redshift – Galaxies: evolution

1. Introduction

Little Red Dots are a new phenomenon discovered by *JWST* (Harikane et al. 2023; Matthee et al. 2024; Kocevski et al. 2024; Killi et al. 2024; Greene et al. 2024) mostly at $z \sim 4$–7, with a rapid drop-off at lower redshift (Park et al. 2026; Lin et al. 2026a). They are spatially compact in the redder filters, have broad H and He lines (Matthee et al. 2024; Greene et al. 2024; Juodžbalis et al. 2025) with exponential shapes (Rusakov et al. 2026), and a spectral break occurring close to the Balmer limit wavelength (Setton et al. 2025; Akins et al. 2024). These properties have been variously argued to be consistent with tidal disruption events (Bellovary 2025), late-stage quasi-stars (Begelman & Dexter 2025), or even supermassive stars (Nandal & Loeb 2025). In general, however, most models now involve accretion onto a supermassive black hole in a high density environment (Inayoshi & Maiolino 2025; Maiolino et al. 2025b). This high density gas cocoon reprocesses radiation from the SMBH accretion, producing strong Balmer (de Graaff et al. 2025b; Naidu et al. 2025; Sneppen et al. 2026a) and Paschen (Sneppen et al. 2026b) features, as well as the electron-scattering broadened permitted lines commonly observed in LRDs (see e.g. Rusakov et al. 2026; Kokorev et al. 2025; Chang et al. 2026; Brazzini et al. 2026; Matthee et al. 2026). This envelope of dense gas is also likely to suppress radio emission and X-rays (Maiolino et al. 2025b; Sneppen et al. 2026c; Comastri et al. 2026; Tortosa et al. 2026), while the high densities can also account for the anomalous Balmer emission observed in LRDs (D'Eugenio et al. 2025a; Yan et al. 2025; Nikopoulos et al. 2026). Radiative transfer simulations in multidimensional, moving gas have successfully reproduced most spectral features, indicating the need for a higher density, slow-moving inflow, and a faster outflow, with column densities of $10^{24.5}$– $10^{25.5}$ cm^{-2} (Sneppen et al. 2026a).

There is an ongoing debate on the precise nature of these sources, with interpretations including a stellar-like photosphere (e.g. Kido et al. 2025; Inayoshi et al. 2025; de Graaff et al. 2025a,b), reminiscent of a quasi-star interpretation (Begelman & Dexter 2025), a supermassive star (Nandal & Loeb 2025) and perhaps related to direct-collapse black hole formation (Pacucci et al. 2026). However, evidence for both inflowing and outflowing gas in many objects (Davis et al. 2026; Matthee et al. 2026) militates against a simple hydrostatic configuration. Moreover, strong emission lines emerging from within the scattering region are difficult to reconcile with a fully reprocessing photosphere. Conversely, pro-

⋆ georgios.nikopoulos@nbi.ku.dk
⋆⋆ darach@nbi.ku.dk

ducing the broad emission lines outside a cool reprocessed atmosphere with $T \lesssim 6000\,\mathrm{K}$ is also challenging (Martins et al. 2026), while the observed line-to-continuum ratios are large and suggestive of a nebular-dominated continuum, even without an additional thermalised component (Sneppen et al. 2026b).

Recent studies of individual LRDs place them in a metal-poor regime (~ 5–15% $Z_\odot$ Greene et al. 2024; Juodžbalis et al. 2024; Killi et al. 2024; Tripodi et al. 2024; D'Eugenio et al. 2025a; Torralba et al. 2026; D'Eugenio et al. 2026; Ivey et al. 2026), although Maiolino et al. (2025a) argue for a very metal-poor counterpart in Abell2744-QSO1. Several observations further indicate that LRDs are not pristine systems, but are surrounded by high–column-density gas that is likely enriched: deep limits on soft X-rays require at least modest photoelectric absorption by metals (Sneppen et al. 2026c), while strong metal absorption features, including Ca II, Na I, and K I, point to substantial cool metal-enriched gas along the line of sight (Lin et al. 2026b; D'Eugenio et al. 2025b; Ji et al. 2026). The possible detection of water-vapour signatures in several low-redshift LRDs (Wang et al. 2026) suggests the presence of dense molecular gas with significant columns of oxygen surrounding these sources.

Despite this mounting evidence for non-pristine, high column density gas, the metal abundances of LRDs and their hosts have not, to date, been systematically measured. The assumptions on the metallicity of LRDs greatly influence the interpretation of their spectra, as well as the results of SED and radiative transfer modelling. In addition, metallicity is a key discriminant between the proposed LRD formation channels, with pristine environments favouring a recent direct-collapse black hole formation scenario (Pacucci et al. 2026), whereas a measurement of substantial enrichment would instead point to a host that has already undergone significant star formation. Therefore, a robust abundance determination would put meaningful constraints on both future modelling of the observed conditions of LRDs and their evolution across cosmic time.

In this work, we present the first catalogue of gas-phase metallicities and temperatures for a sample of LRD hosts observed with medium and high resolution JWST/NIRSpec spectroscopy. We derive metallicities through the classical direct T_e method, and cross-check them against widely used strong line calibrations in the literature ($\hat{R}$, R23, O32, Ne3O2 and N2). We also provide the first comparison between the results derived using grating and low resolution NIRSpec PRISM spectroscopy. Throughout the paper we adopt a solar oxygen abundance of 12+log(O/H) = 8.69 (Asplund et al. 2009) when converting to $Z/Z_\odot$. The paper is organised as follows. In Section 2 we describe the observational sample and its selection; in Section 3 we present our line-fitting procedure and the direct T_e and strong line calibration frameworks; in Section 4 we report our results on the temperatures and metallicities of LRDs, before discussing their implications on the nature of LRDs in Section 5. We summarise our findings in Section 6.

2. Observational samples

We use data from the DAWN *JWST* Archive (DJA) (de Graaff et al. 2025c; Pollock et al. 2026; Heintz et al. 2025), where objects from previous LRD samples are included (e.g. Barro et al. 2025; de Graaff et al. 2025b; Pérez-González et al. 2026; Sneppen et al. 2026a; Matthee et al. 2026). The data are publicly available from several *JWST* observing programmes using the NIRSpec spectrograph (Jakobsen et al. 2022) with the following Programme IDs: 1180, 1181, 1286 (JADES; Eisenstein et al. 2026), 1212 (GTO WIDE; Maseda et al. 2024) 9223 (PI: S. Fujimoto, Atek et al. 2025), 3567 (DEEP-DIVE; Ito et al. 2025), 4233 (RUBIES; de Graaff et al. 2025d), 1345 (CEERS; Finkelstein et al. 2023), 4106 (PI: E. Nelson, Nelson et al. 2023), 4287 (PI: C. Mason, Mason et al. 2023; Whitler et al. 2026, LRD observations presented in Tang et al. 2025) and 9214 (SPURS; PIs: C. Mason & D. Stark, Chen et al. 2026). We use the LRD sample to be presented in Nikopoulos et al. (in prep.). This sample is the same as that used in the updated paper by Sneppen et al. (2026a). In brief, this sample of LRDs is selected using color, compactness, and the presence of broad Hα lines. The color selection requires either a significant Balmer break ($D_{4000} = F_{4200\text{Å}}/F_{3500\text{Å}} > 1.2$, following Binggeli et al. 2019), which measures the strength of the hydrogen-related spectral discontinuity at 4000 Å, or a strong change in spectral slope between the ultraviolet and optical ($\beta_{\rm UV} < -0.2, \beta_{\rm opt} > 0, \beta_{\rm opt} - \beta_{\rm UV} > 0.5$ following de Graaff et al. 2025b). Compactness is assessed using Sérsic profile fits in the $F444W$ filter. The presence of broad emission lines is quantified using the Bayesian Information Criterion (BIC), requiring ΔBIC > 10 in favor of a model that includes a broad-line component.

3. Methods

We interpret the Balmer emission in LRDs as consisting of an intrinsic line core plus exponential wings produced by electron scattering through a Compton-thick medium (Rusakov et al. 2026). In this picture, the source is a central engine, such as an accreting supermassive black hole, embedded within a cocoon of highly dense, ionised gas (Rusakov et al. 2026; Naidu et al. 2025; de Graaff et al. 2025e; Inayoshi & Maiolino 2025; Sneppen et al. 2026a). We decompose the Balmer line profiles into a narrow component representing emission from the host galaxy (and/or a possible Narrow Line Region, NLR), and a broad component. The broad component consists of the sum of an 'unscattered' and a 'scattered' component, modelled respectively as a simple Gaussian, and a Gaussian with the same width convolved with an exponential. Where necessary, an absorption component is mutiplied by this model to account for the absorption lines frequently detected in LRD spectra. For a more detailed analysis of the fitting model adopted, the reader is referred to Rusakov et al. (2026); Nikopoulos et al. (2026).

We use the fiducial model outlined above to fit the all the Hα lines in our sample. The width and redshift of the narrow Balmer components are tied to those of the [O III] 4959,5007Å doublet in velocity space, with each parameter having flat priors whose limits are dictated by the [O III] 4959,5007Å fit uncertainties. The broad Hβ, Hγ, and Hδ profiles are scaled to match the respective components of the Hα profiles, except in rubies-egs61_4233_55604, rubies-egs63_4233_49140, and jades-gdn2_1181_28074, where the Hβ broad components statistically prefer an independent fit. All line widths are corrected for the instrumental resolution, for which we adopt an effective spectral resolution that is 1.7 times better than the nominal value reported in the NIRSpec documentation, following instrument modelling of point sources presented in the literature (de Graaff et al. 2024). Using a different effective resolution does not alter the fluxes inferred, and therefore the results of this work are largely unaffected by this choice, as shown in Nikopoulos et al. (2026).

In this work, we use `dynesty` v.2.1.5 (Speagle 2020; Koposov et al. 2024) with static nested sampling (Skilling 2004; Skilling 2006), adopting 150n live points, where n is the number of free parameters. To explore complex posterior distributions efficiently, we employ random-walk sampling (Skilling 2004) together with multi-ellipsoidal bounding (Feroz et al. 2009) around the live points, which helps to capture degeneracies and multimodal structure. We then use the posterior samples from `dynesty` to compute flux distributions for all components and emission lines. The best fit fluxes represent the median of the retrieved distribution, while the uncertainties given are to the 16th and 84th percentiles. We consider a line/component to be detected when its flux exceeds zero by more than 3σ, while a 2σ limit is quoted in case of a non-detection. We present the fluxes estimated in this work for all objects in Table A.1. All measurements presented are made by propagating each line flux's posterior probability distribution, using only narrow components/lines. We did not attempt to determine the metal abundances using the broad lines, as the regions from which this emission arises are almost certainly above the critical densities of the forbidden metal lines.

3.1. Direct T_e: Deriving electron temperatures and elemental abundances

The gas-phase metallicities were derived with a classical direct T_e framework using `PyNeb` (Luridiana et al. 2015; Morisset et al. 2020). For each source, posterior probability flux distributions were assembled for the [O III] 4959,5007 Å, [O III] 4363 Å, [O II] 3726,3729 Å, and Hβ narrow component. Electron temperatures were computed from the nebular-to-auroral oxygen ratio, $R_{\rm OIII} = \frac{I(4959)+I(5007)}{I(4363)}$, adopting fixed-density runs at a range of electron densities of $n_e = 10^2$ - 10^6 cm^{-3}. All results quoted in this paper correspond to the case of $n_e = 10^2$ cm^{-3}. The resulting T_e posteriors were retained per object, including an upper limit flag when the [O III] 4363 Å line was not significantly detected. The posteriors were then propagated to compute oxygen abundances as $\frac{\rm O}{\rm H} = \frac{\rm O^+}{\rm H} + \frac{\rm O^{++}}{\rm H}$.

For object IDs glimpse-obs01_9223_12248, glimpse-obs01b_9223_5536, rubies-uds3_4233_47509, there is no grating coverage of the [O II] 3726,3729 Å lines. These objects show temperatures greater than 20000 K, however (see Table 1). The average [O III] 4959,5007 Å/[O II] 3726,3729 Å ratios of other similarly hot objects in the sample, for which the [O II] 3726,3729 Å doublet is detected, are 17^{+21}_{-10}. Thus, for these objects, the O$^+$ ionization state was neglected, since its average contribution to the total oxygen abundance is expected to be minimal.

We note that we use all narrow Balmer line components available per object to estimate the narrow line A_V using the `dust_extinction` module (Gordon 2024) and assuming an SMC extinction curve (Gordon et al. 2024). We find that for most (though not all) objects, $A_V = 0$ within 1σ. (We caution, however, that narrow line Balmer decrements are poorly constrained due to degeneracies in the line-core decomposition of Balmer lines.) Other works also indicate minimal dust in the host galaxy emission (e.g. Killi et al. 2024; Matthee et al. 2024; Brooks et al. 2025; Zhang et al. 2026b; Nikopoulos et al. 2026). We therefore only extinction-correct objects whose estimated narrow-component A_V exceeds 0 at $> 3\sigma$. Specifically, we note that objects jades-gds06_1286_159717 and jades-gdn2_1181_28074 show $A_V = 1.4 \pm 0.2$, and $A_V = 2.0 \pm 0.1$, respectively. A bigger systematic analysis of the dust emission of the full sample is left for future work.

3.2. Strong line diagnostics

We also used the estimated fluxes to calculate several strong line diagnostics, which are widely used in the literature to constrain the metallicities of high-z star-forming galaxies, and are defined as follows:

$$\begin{aligned}
\mathrm{R23} &= ([\mathrm{O\,III}]\,4959{,}5007\,\text{Å} + [\mathrm{O\,II}]\,3726{,}3729\,\text{Å})/\,\mathrm{H}\beta,\\
\mathrm{O3} &= [\mathrm{O\,III}]\,5007\,\text{Å}/\,\mathrm{H}\beta,\\
\mathrm{O2} &= [\mathrm{O\,II}]\,3726{,}3729\,\text{Å}/\,\mathrm{H}\beta,\\
\mathrm{O32} &= [\mathrm{O\,III}]\,5007\,\text{Å}/\,[\mathrm{O\,II}]\,3726{,}3729\,\text{Å},\\
\mathrm{Ne3O2} &= [\mathrm{Ne\,III}]\,3869\,\text{Å}/\,[\mathrm{O\,II}]\,3726{,}3729\,\text{Å}, \text{ and}\\
\hat{\mathrm{R}} &= 0.47\log(\mathrm{O2}) + 0.88\log(\mathrm{O3}).
\end{aligned}$$

We compared our direct T_e metallicities against R_{23}, the projected $\hat{\mathrm{R}}$ indicator, O32, and Ne3O2, using the relations from Scholte et al. (2025) and Sanders et al. (2026). The $\hat{\mathrm{R}}$ and N2 = [N II] 6583 Å/ Hα calibrations were also used to estimate the metallicity for all objects in the sample for comparison purposes, using the inverse relations from Scholte et al. (2025) and Sanders et al. (2026) respectively, while taking into account the intrinsic scatter of every relation. We used the $\hat{\mathrm{R}}$ calibration in Scholte et al. (2025), as its low metallicity (12 + log(O/H) < 7.2) extrapolation provides a more suitable fit to the estimated line ratios of similarly enriched objects. However, we note that the $\hat{\mathrm{R}}$ relation presented in Sanders et al. (2026) is completely consistent with the relation we used in this work for 6.8 < 12 + log(O/H) < 8.2, which is the regime that most LRDs in the sample lie in (see Sec. 4.1). We finally use N2 as an informative prior on the direct T_e metallicity, to truncate the high-O/H tail of the direct T_e posterior.

4. Results

4.1. Direct T_e gas temperatures and metallicities

Across the grating sample, we recover a broad range of electron temperatures $\mathrm{T_e} \sim 15\,000$–$45\,000$ K. Specifically, we find that the modes of the derived temperature distributions for 18/22 direct T_e objects lie well below 30 000 K, in broad similarity with ISM conditions of high-redshift star-forming systems (see e.g. Laseter et al. 2024; Morishita et al. 2024; Chakraborty et al. 2025; Nishigaki et al. 2025; Pollock et al. 2026; Sanders et al. 2024, 2026). We note that a significant fraction of the sample lacks a robust [O III] 4363 Å line detection; for those objects we quote 2σ upper limits on the electron temperature, which translate into lower limits on the derived oxygen abundance.

The resulting metallicities span a range of 0.05–0.2 $Z_\odot$, indicating that gas in LRDs is metal-poor. We find that the mode of the metallicity distribution of the bottom 80% the objects lies below 0.1 $Z_\odot$, while the mode of the remaining 20% is less than 0.2 $Z_\odot$. The T_e, as well as the metallicities derived for the full sample can be found in Table 1. We also plot a contour map of the combined derived T_e and metallicity distributions of all objects in Figure 1, and we report an average $Z_{T_e} = 0.08^{+0.11}_{-0.03}\,Z_\odot$ and $T_e = 23000^{+17000}_{-7000}$ K for our sample. In Figure 2, we present the stacked direct T_e metallicity posteriors of the full sample. Our results then indicate that the gas in LRDs is indeed metal poor, but nowhere near pristine conditions. We have assumed a moderate density (100 cm^{-3}) throughout our analysis, in accordance with the range of densities inferred for LRDs at low z (Lin et al. 2026a). We note that since the oxygen abundance is dominated by the [O III] 4959,5007 Å flux, which has a critical density of $n_e \sim 7 \times 10^5$ cm^{-3} (Baskin & Laor 2005), increas-

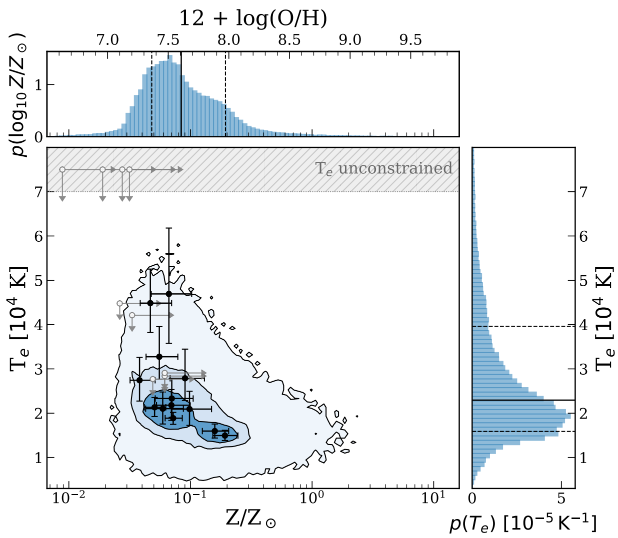

Fig. 1: Metallicities and electron temperatures from the direct T_e method, for the full sample. The 39th, 68th and 95th percentile contours of the combined posterior probability distributions for the sample are shown in the central panel, with histograms of the one dimensional distributions shown on their respective axes. Median values are indicated with a solid line and 1σ intervals with dashed lines.

ing the density up to 10^4 cm^{-3} does not alter our results. Different densities could not make the metal abundances significantly lower than we derive, so that our conclusions on non-pristine gas are robust. However the inferred abundance could increase by ~ 0.3 dex (a factor of two in solar units) if very high densities (10^5 cm^{-3}) are assumed for the narrow lines. While this seems extreme for the hosts of LRDs, there is some evidence of such high densities in three [O III]-emitting regions in star-forming galaxies at $z = 6.1$, 6.1, and 7.0, (Arellano-Córdova et al. 2026), so such high densities cannot be ruled out at present. On the other hand, even allowing for a 0.3 dex upward shift in the $z \gtrsim 5$ objects in our sample would not greatly affect our conclusions. Furthermore, we detect significant [O II] 3726,3729 Å emission in nine objects out of 22 measured in the sample. At 10^5 cm^{-3} the [O II] 3726,3729 Å would be strongly suppressed. The measurements we have, give O32 ratios and lower bounds between 4 and 20, which suggest a density for a single-zone medium that is not far above the critical density for [O II] 3726,3729 Å, $\sim 10^4$ cm^{-3}. Of course a multi-zone medium would allow this constraint to be evaded.

We also find objects with unconstrained temperature upper limits, due to a combination of relatively weak [O III] 4959,5007 Å emission, and a relatively high [O III] 4363 Å line 2σ upper limit. These flux limits then yield temperature ranges that extend into the asymptotic regime of the [O III] 4959,5007 Å/ [O III] 4363 Å vs T_e relation (Osterbrock & Ferland 2006). This is due to the limitations of the data with respect to the detection of the [O III] 4363 Å line. For these objects, we use the R̂ calibration, as a proxy for their metallicity, since it provides a measurement that is in general consistent with the direct T_e method (see Fig. 2).

4.2. Strong line calibration metallicities

Comparing our direct T_e metallicities against the widely used strong-line diagnostics shows that the bulk of our sample is broadly consistent with these calibrations (see Fig. 3). R_{23} and R̂ track the direct T_e values most tightly, reflecting their weaker sensitivity to the ionization state of the gas, whereas O32 and Ne3O2 display noticeably larger scatter.

The tightest and therefore most informative correlation is found with the R̂ diagnostic both for the population (Fig. 2), as well as for individual objects (see top-left panel, Fig. 3). The bulk of the population lies in the lower R̂-metallicity branch ($Z < 0.3\,Z_\odot$) avoiding the ambiguity of the high-metallicity branch. We thus derive the metallicities of LRDs using the R̂ calibration, and plot the combined R̂ metallicity posteriors for all objects in the sample, in Fig. 2. We compute an average $Z_{\hat{R}} = 0.07^{+0.07}_{-0.04}\,Z_\odot$, in agreement with the average derived for the direct T_e method. It is noted that the highest likelihood R̂ metallicities are marginally higher than their direct T_e counterparts. As discussed in Section 5.2, LRDs have temperatures that are consistent with the hotter branch of high z SF galaxies. Since the R̂ vs. metallicity relation has been calibrated against such systems, a high redshift galaxy with the same R̂ value can be expected to have marginally lower temperature and therefore higher metallicity than a typical LRD. Nevertheless, the metallicities inferred are not affected, since 11/13 objects have consistent direct T_e and R̂ metallicities within 1σ, while the remaining two are reconciled at $< 2\sigma$. The insignificance of that effect is further corroborated by the fact that the R̂ metallicity posterior does not have a very high metallicity tail, as seen in the direct T_e posterior. This direct T_e tail is driven by non-detections of the [O III] 4363 Å line, leading to low inferred temperatures, and thus

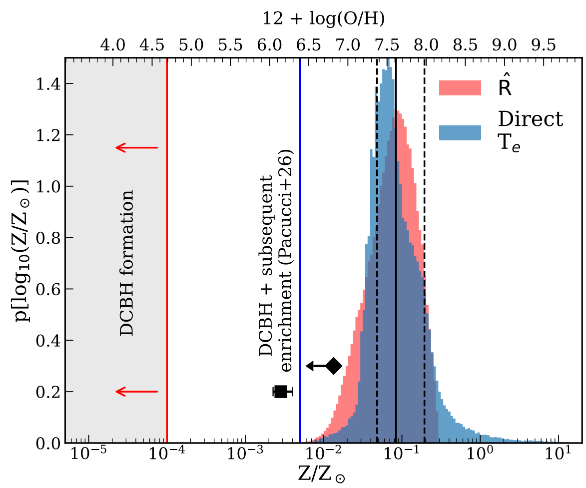

Fig. 2: Summed posterior probability distributions of the metallicities determined using the direct T_e (blue) and R̂ (red) methods. Both methods suggest sub-solar metallicities with, $Z_{T_e} = 0.08^{+0.11}_{-0.03}\,Z_\odot$ and $Z_{\hat{R}} = 0.07^{+0.07}_{-0.04}\,Z_\odot$. R̂ metallicity estimates for abell2744-spurs02_9214_41 (diamond) and jades-gds-w09_1212_2993 (square) are shown separately and are placed in arbitrary y axis values. The theoretical limits for DCBH formation from near-pristine gas (red line) and DCBH formation plus subsequent enrichment to the LRD phase (blue line) are shown (Pacucci et al. 2026). Most of the sample is incompatible with these limits.

Table 1: Estimated temperatures and metallicities for all methods used.

ID	Object	z	12 + log(O/H) [T_e]	T_e [K]	12 + log(O/H) [$\hat{R}$]	12 + log(O/H) [N2]	DT_e+N2	$Z/Z_\odot$
1	abell2744-spurs02_9214_41	7.037	—	—	< 6.81	—	—	—
2	rubies-egs61_4233_55604	6.983	$7.36^{+0.17}_{-0.08}$	44800^{+7700}_{-6600}	$7.46^{+0.29}_{-0.25}$	—	$7.36^{+0.17}_{-0.08}$	$0.05^{+0.02}_{-0.01}$
3	rubies-uds42_4233_807469	6.775	> 7.13	< 74000	$7.29^{+0.30}_{-0.26}$	—	> 7.13	> 0.03
4	jades-gdn2_1181_954	6.760	$7.54^{+0.18}_{-0.14}$	23300^{+4600}_{-4300}	$7.41^{+0.26}_{-0.23}$	< 8.10	$7.55^{+0.17}_{-0.14}$	$0.07^{+0.04}_{-0.02}$
5	egs-nelsonx_4106_47962	6.728	$7.46^{+0.17}_{-0.14}$	21000^{+3800}_{-3500}	$7.28^{+0.23}_{-0.21}$	< 8.18	$7.48^{+0.17}_{-0.15}$	$0.06^{+0.03}_{-0.02}$
6	rubies-egs63_4233_49140	6.685	$7.51^{+0.19}_{-0.15}$	46900^{+14900}_{-11200}	$7.59^{+0.26}_{-0.25}$	< 7.98	$7.50^{+0.17}_{-0.14}$	$0.06^{+0.03}_{-0.02}$
7	glimpse-obs01b_9223_5536	6.223	> 7.19	—	$7.71^{+0.22}_{-0.22}$	—	> 7.19	> 0.03
8	glimpse-obs01_9223_12248	6.108	$7.39^{+0.09}_{-0.08}$	21300^{+2200}_{-2100}	$7.63^{+0.22}_{-0.19}$	< 8.06	$7.40^{+0.09}_{-0.09}$	$0.05^{+0.01}_{-0.01}$
9	jades-gdn_1181_38147	5.869	$7.53^{+0.15}_{-0.12}$	21800^{+3500}_{-3400}	$7.61^{+0.22}_{-0.20}$	< 8.23	$7.69^{+0.20}_{-0.19}$	$0.10^{+0.06}_{-0.03}$
10	rubies-uds3_4233_47509	5.672	> 7.38	< 27700	$7.78^{+0.19}_{-0.19}$	< 7.80	$7.71^{+0.22}_{-0.21}$	$0.10^{+0.07}_{-0.04}$
11	ceers_1345_746	5.622	> 6.64	—	> 7.21	< 8.46	$7.22^{+0.53}_{-0.36}$	$0.03^{+0.08}_{-0.02}$
12	jades-gds05_1286_204851	5.482	> 7.48	< 29100	$7.68^{+0.22}_{-0.23}$	< 7.98	$7.82^{+0.22}_{-0.21}$	$0.14^{+0.09}_{-0.05}$
13	ceers-egs_1345_2782	5.239	> 7.21	< 42200	$7.33^{+0.33}_{-0.29}$	—	> 7.21	> 0.03
14	jades-gds06_1286_159717	5.077	$7.68^{+0.18}_{-0.15}$	20900^{+4000}_{-3700}	$7.82^{+0.17}_{-0.19}$	< 7.94	$7.68^{+0.15}_{-0.14}$	$0.10^{+0.04}_{-0.03}$
15	jades-gdn_1181_68797	5.039	$7.43^{+0.15}_{-0.11}$	32700^{+6800}_{-5100}	$7.78^{+0.19}_{-0.20}$	< 8.38	$7.73^{+0.27}_{-0.27}$	$0.11^{+0.09}_{-0.05}$
16	valentino-egs_3567_42232	4.952	> 6.97	—	$7.33^{+0.32}_{-0.28}$	< 8.00	$7.31^{+0.26}_{-0.21}$	$0.04^{+0.03}_{-0.02}$
17	jades-gdn_1181_39353	4.849	> 7.11	< 44900	$7.21^{+0.30}_{-0.26}$	< 7.92	$7.49^{+0.31}_{-0.26}$	$0.06^{+0.07}_{-0.03}$
18	jades-gds-w09_1212_2993	4.824	—	—	$6.15^{+0.15}_{-0.10}$	< 8.24	—	—
19	jades-gds02_1286_38562	4.821	$7.89^{+0.11}_{-0.10}$	16000^{+1600}_{-1600}	$7.67^{+0.22}_{-0.20}$	< 7.90	$7.86^{+0.10}_{-0.09}$	$0.15^{+0.04}_{-0.03}$
20	ceers-egs_1345_1244	4.477	$7.97^{+0.11}_{-0.10}$	14900^{+1200}_{-1100}	$7.67^{+0.22}_{-0.21}$	$8.12^{+0.09}_{-0.11}$	$8.05^{+0.07}_{-0.08}$	$0.23^{+0.04}_{-0.04}$
21	jades-gdn_1181_73488	4.133	$7.27^{+0.13}_{-0.08}$	27400^{+5200}_{-4700}	$7.07^{+0.19}_{-0.19}$	< 8.12	$7.32^{+0.17}_{-0.11}$	$0.04^{+0.02}_{-0.01}$
22	jades-gds-wide_1180_13329	3.938	> 7.48	< 28400	$7.81^{+0.18}_{-0.20}$	< 8.21	$7.88^{+0.21}_{-0.20}$	$0.16^{+0.10}_{-0.06}$
23	jades-gdn_1181_53501	3.429	$7.65^{+0.16}_{-0.12}$	27900^{+6600}_{-5000}	$7.67^{+0.24}_{-0.26}$	< 7.86	$7.63^{+0.14}_{-0.12}$	$0.09^{+0.03}_{-0.02}$
24	jades-gdn2_1181_28074	2.260	$7.55^{+0.07}_{-0.07}$	18900^{+1300}_{-1400}	$7.63^{+0.22}_{-0.19}$	$7.64^{+0.06}_{-0.09}$	$7.59^{+0.06}_{-0.06}$	$0.08^{+0.01}_{-0.01}$

Notes. Abundances were estimated assuming an electron density of 10^2 cm^{-3}. Upper limits on the temperature arise if the [O III] 4363 Å line is not detected. Upper limits exceeding 10^5 K are marked with '—'. Objects with no [N II] 6583 Å and Hα narrow component detections have no meaningful N2 estimate, and are also denoted with '—'. The final column quotes the combination of the direct T_e and N2 metallicities in solar units.

high metallicities. The $\hat{R}$ calibration is better constrained in that sense, since it does not depend on the usually faint [O III] 4363 Å line. We therefore argue that the $\hat{R}$ can be safely used to estimate the metallicity of LRDs, if the direct T_e method is not feasible.

The [N II] 6583 Å line is not detected in 22 out of 24 objects in the sample; the N2-derived abundances are then quoted as upper limits where the Hα narrow component is detected, and are found to be broadly consistent with the direct T_e method abundances. N2 is strongly sensitive to the ionization parameter (Morales-Luis et al. 2014) and to any AGN contribution to the flux of the [N II] 6583 Å line, while star-forming galaxies at high redshift show moderate to extreme nitrogen enrichment (e.g. Bunker et al. 2024; Cameron et al. 2023; Isobe et al. 2023; Zhang et al. 2026a; Cataldi et al. 2025; Cameron et al. 2026). As a consequence, N2-based abundances are conservative when used as an upper bound, and can be used to independently constrain the high O/H tail of our direct T_e posteriors. Indeed, the combined direct T_e and N2 posteriors show on average lowered upper bounds, yielding $Z_{joint} = 0.08^{+0.09}_{-0.04}\,Z_\odot$ for the full sample. The above population average is consistent with the values obtained using both the direct T_e method and the $\hat{R}$ calibration. The results of all methods presented in this work can be found in Table 1.

4.3. Evidence for extremely metal poor LRDs

In this section we highlight two objects in the sample, abell2744-spurs02_9214_41 (A2744-QSO1, $z = 7.04$; Maiolino et al. 2025a and jades-gds-w09_1212_2993 ($z = 4.88$, de Graaff et al. 2025b).

Abell2744-spurs02_9214_41 has been extensively discussed in the literature (Maiolino et al. 2025a; Juodžbalis et al. 2026; Tang et al. 2026) and was reported to have $Z = 0.0047\,Z_\odot$ in its central region, while an extended region of 200 pc around its core shows $Z < 0.0039\,Z_\odot$ (Maiolino et al. 2025a). Indeed, we report that in this object all oxygen lines are non-detections, making a direct T_e measurement impossible. We then use the $\hat{R}$ strong line calibration, and put a 2σ upper limit on its metallicity of $Z < 1.3\%\,Z_\odot$, consistent with previous findings.

Jades-gds-w09_1212_2993 shows no detected emission line at 3σ apart from Hα, in all grating spectra available. We nevertheless use the Hα profile derived from fitting the available G395H spectrum in the DJA, to decompose the Hβ +[O III] 4959,5007 Å complex in the PRISM spectrum, which has much higher SNR. We are then able to estimate the narrow Hβ and [O III] 5007 Å fluxes, and thus use the O3 strong line calibration to estimate a metallicity of $Z = 0.0034^{+0.0010}_{-0.0008}\,Z_\odot$. This is consistent with the corresponding $\hat{R}$ measurement, $Z = 0.0029^{+0.0011}_{-0.0006}\,Z_\odot$. This result firmly puts Jades-gds-w09_1212_2993 as one of the most metal poor LRDs discov-

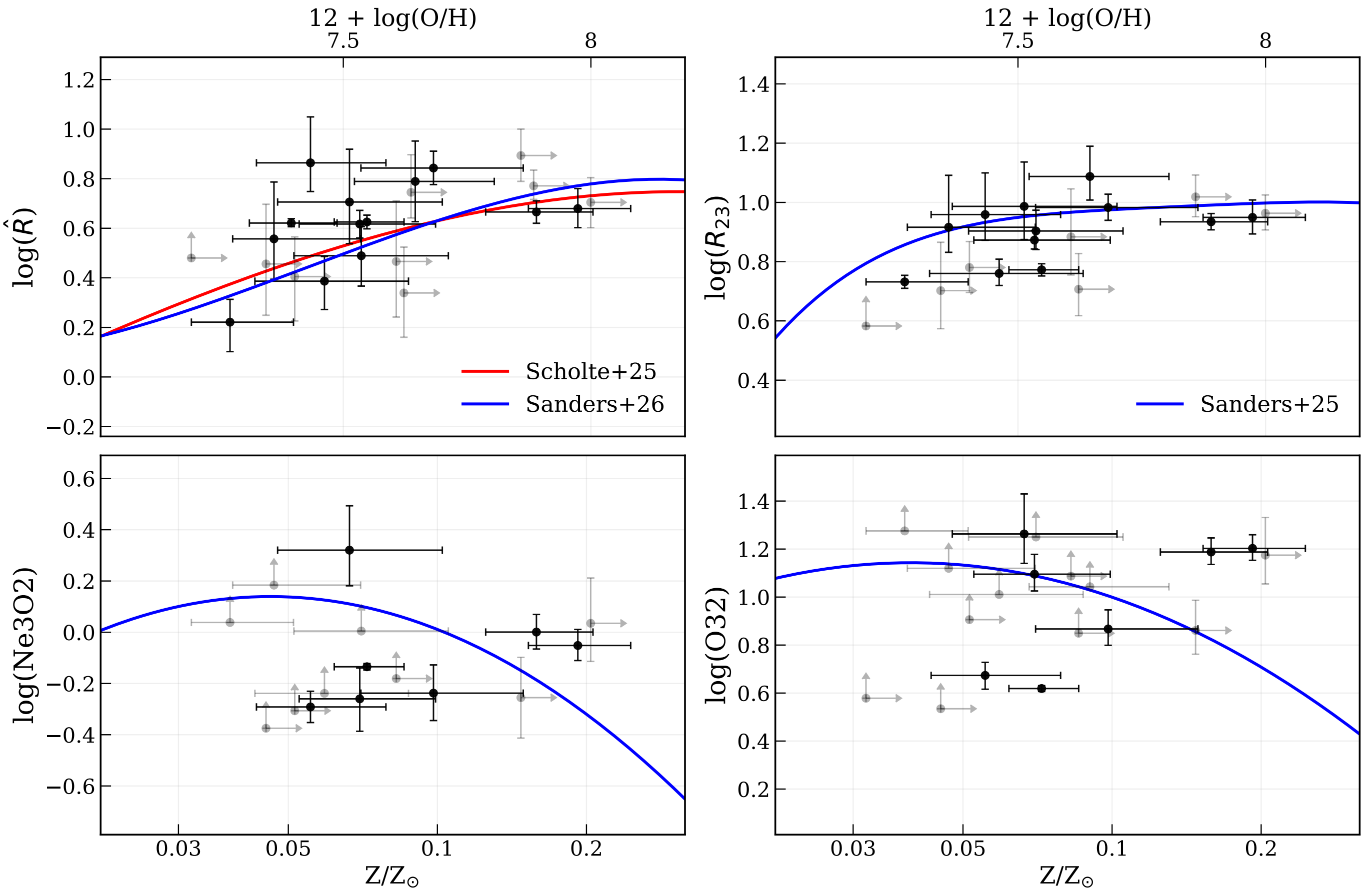

Fig. 3: Strong line calibration ratios vs. direct-T_e metallicities. We also plot the empirical calibrations from Scholte et al. 2025 (red) and Sanders et al. 2026 (blue) derived using high-z star forming systems with [O III] 4363 Å detections.

ered to date, with significant implications on the formation scenarios of LRDs (Fig. 2). We nevertheless caution that the use of PRISM low resolution spectra, under incorrect assumptions or certain redshift regimes, can lead to very different results when compared to the full direct T_e method, utilizing medium/high resolution spectra (see Sec. 4.4).

4.4. Comparison of grating- and PRISM-derived metallicities

In this subsection, we test whether the results derived in this work match with abundances derived using NIRSpec PRISM spectra. To this end, we perform a very simple analysis of the PRISM spectra of objects in our sample which have medium/high-resolution-derived metallicities, in which 1) we fit Balmer lines with broad components which do not take into account any quantities derived using grating spectra, 2) we neglect the possibility of a broadened [O III] 4363 Å line, as found in rubies-egs63_4233_49140 (Nikopoulos et al. 2026; D'Eugenio et al. 2025a) and 3) we assume all lines are detected. The latter criterion is forced so that the methodology emulates the results of automated fitting routines, like `msaexp` (Brammer 2023). We then perform the same method detailed in Section 3 to derive the PRISM-based metallicities, and compare them with the grating-based metallicities in Figure 4.

In the sample of 8 objects for which the metallicity reported is not a lower limit, and for which PRISM spectra are available, 5 out of 8 objects show an inconsistency between the values derived using grating and PRISM spectra. For 3 out of 5 objects, this inconsistency is reconciled at 2σ, while jades-gdn_1181_68797 and jades-gds06_1286_159717 are reconciled at 3σ.

The above inconsistencies suggest that PRISM spectra might not have sufficient resolution to accurately decompose the Hβ + [O III] 4959,5007 Å, and the Hγ + [O III] 4363 Å complexes, and retrieve the various fluxes safely. In order to quantify the deviation between the two sets of measurements, we calculate the distribution of ratios of the oxygen abundance derived using PRISM, 12 + log(O/H)$_{\rm PRISM}$ over the one derived using grating spectra, 12 + log(O/H)$_{T_e}$, for objects with [O III] 4363 Å line detections in the grating spectra. We find that the median ratio of the distribution is indeed 1.03, with a 1σ scatter of 7%. This effectively means that for an object with the average metallicity of the sample, 12 + log(O/H) = 7.59 (Z = 0.08 Z$_\odot$), the PRISM estimate can be off by up to 0.8 dex at 1σ, leading to possible measurements anywhere between 0.05 Z$_\odot$ and 0.54 Z$_\odot$. For comparison purposes, the median and scatter of the equivalent distribution of (12+log(O/H)$_{\hat{\rm R}}$)/(12+log(O/H)$_{T_e}$) is 1 ± 4%. We note that if one includes a 3σ non-detection threshold in the PRISM analysis, there are only 3 objects which have both constrained grating and PRISM metallicity measurements, with all 3 being inconsistent. The process of deriving the median ratio and scatter between the two sets, described above, is independent on

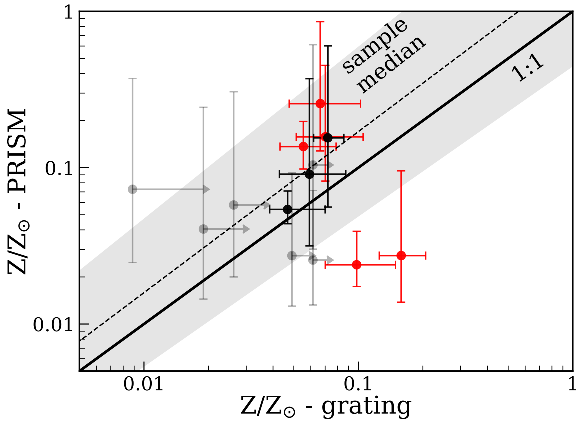

Fig. 4: Direct T_e metallicities from PRISM spectra compared to direct T_e metallicities from grating spectroscopy. The solid line shows the region on which the two metallicities are equal. The dashed line and shaded region correspond to the average observed PRISM/grating metallicity relation and 1σ scatter of $1.03 \pm 0.07\%$ in 12+log(O/H) space. Faded gray objects correspond to those whose grating metallicity estimation is a lower limit due to the non-detection of the [O III] 4363 Å line. Data points coloured red signify objects for which the two measurements are not in agreement within 1σ.

whether a line is treated as an upper limit or not, and therefore holds irrespective of the detection threshold adopted.

We argue then that PRISM data could yield a sufficiently reliable metallicity estimate on individual objects, assuming that the resolution and SNR are sufficient to resolve the blends of Balmer and oxygen lines, and that the analysis is sophisticated enough and tailored to the object under investigation. On the other hand, caution should be exercised when using metallicity estimates of PRISM-based LRD sample studies, unless their analyses fulfill the above criteria.

5. Discussion

5.1. On the metallicity of LRDs

In this work, we provide the first metallicity estimate which uses medium and high resolution spectra for a sample of 24 LRDs. Our sample-averaged direct-T_e abundance of $Z = 0.08^{+0.11}_{-0.03}\,Z_\odot$ (Sec. 4.1) places the LRDs firmly in the metal-poor, but not pristine, regime of high-redshift star-forming galaxies. The electron temperatures span $T_e \approx 15000$–45000 K, with the lowest values (~ 16000–21000 K) corresponding to the most enriched objects (jades-gds02_1286_38562; 12+log(O/H) = $7.89^{+0.11}_{-0.10}$ and ceers-egs_1345_2782; 12+log(O/H) = $7.97^{+0.11}_{-0.10}$), and the highest ($\gtrsim$ 30000K) generally reflecting more metal poor conditions (e.g. rubies-egs61_4233_55604 at $z = 6.98$ with 12 + log(O/H) = $7.36^{+0.13}_{-0.08}$). The above metallicity regime overlaps with values measured using the direct T_e method, reported for individual high z LRDs (e.g. Juodžbalis et al. 2024; jades-gdn2_1181_28074 at $\sim 0.15\,Z_\odot$ and D'Eugenio et al. 2025a; rubies-egs63_4233_49140 at roughly 8% $Z_\odot$ although with hints of a metallicity gradient due to density stratification). The derived population properties are also consistent with metallicity estimates for individual objects with grating spectroscopy that use strong-line calibrations. Specifically, Ivey et al. (2026) report 12+log(O/H) $\approx 6.93^{+0.07}_{-0.09}$ for the Cliff at $z = 3.55$, and Maiolino et al. (2024) report 12 + log(O/H) $\approx$ 6.4 for A2744-QSO1 at $z = 7.04$, which lie at, and below the metal-poor tail of our distribution respectively. We finally report broad consistency with the metallicities derived for LRDs from other PRISM-based analyses in the literature (e.g. Killi et al. 2024; Greene et al. 2024; Tripodi et al. 2024).

By comparison, the metallicities of the low-redshift LRD analogues of Lin et al. (2026b) are similar: three objects show metallicities and temperatures at 0.05–0.2 $Z_\odot$ and $T_e \sim$ 14100–24000 K, estimated using the direct T_e method. Lin et al. (2026a) also report 27 LRDs at $z \sim 0.2$–0.9, and argue that their narrow line ratios indicate a mixture of star formation and AGN emission at that redshift ($T_e > 20000$ K). Their measurements suggest metallicities in the range 10%–25% $Z_\odot$, with a population average of 13% $Z_\odot$, assuming a constant $T_e = 15000$ K. We note that the results of this work (see Fig. 1) suggest that the typical temperatures of LRD hosts may be higher; by adopting $T_e \sim 25000$ K instead, the metallicities of the Lin et al. (2026a) DESI sample would drop to a range of 5%–10% $Z_\odot$, as suggested by Fig.1, bringing them in line with the bulk of the sample presented in this work. The consistency of the results of this work with LRDs at $z < 0.9$, suggests that there is minimal evolution in the enrichment of LRDs across cosmic time (see Fig. 5).

Several formation scenarios for LRDs have invoked initially pristine gas conditions, such as required for direct collapse black hole formation, $Z/Z_\odot \lesssim 10^{-5}$–$10^{-4}$ (Omukai et al. 2008; Cenci & Habouzit 2025). Subsequent enrichment could increase the metallicity up to $5 \times 10^{-3}\,Z_\odot$ (Pacucci et al. 2026). Importantly, only 2/24 objects show metallicities naively in agreement with such a scenario (although see caveats discussed in Sec. 4.3). These objects represent just 8% of the sample. Other results in the literature are in agreement with the population average found in this work for the direct T_e method, and seem to be inconsistent with the hypothesis that LRDs exist in extremely metal-poor or even pristine environments. However, these measurements only disfavor models in which the actively observed LRD phase occurs in chemically pristine gas, and may not necessarily rule out all pristine gas formation scenarios.

One thing worth highlighting is an implicit tension in the scenario where Lyman-Werner radiation from a nearby star-forming region is required so as to allow only atomic cooling to prevent fragmentation and thus allow the formation of a supermassive star or a DCBH from pristine gas. Recently it has been argued that at least 43% of LRDs currently have a blue emitting 'blob' close enough to the LRD to provide this radiation (Baggen et al. 2026). At the same time, our results show that most LRD hosts are metal-enriched. For the blue blobs near the LRDs to have prompted the collapse of the object from pristine gas, the metal enrichment would have to happen after the blue blob starts emitting, with the enrichment timescale being significantly shorter than the lifetime of the star-forming blob, so that the blob is still observable.

5.2. Comparison with high redshift star forming galaxies

In Fig. 5 we show the direct T_e oxygen abundances and electron temperatures derived in this work as a function of redshift, overlaid on a compilation of direct T_e measurements for high-z star-forming galaxies selected based on the detection of the [O III] 4363 Å line (Laseter et al. 2024; Morishita et al. 2024; Sanders et al. 2024; Scholte et al. 2025; Pollock et al. 2026; Sanders et al. 2026). To guide the comparison, we also plot the

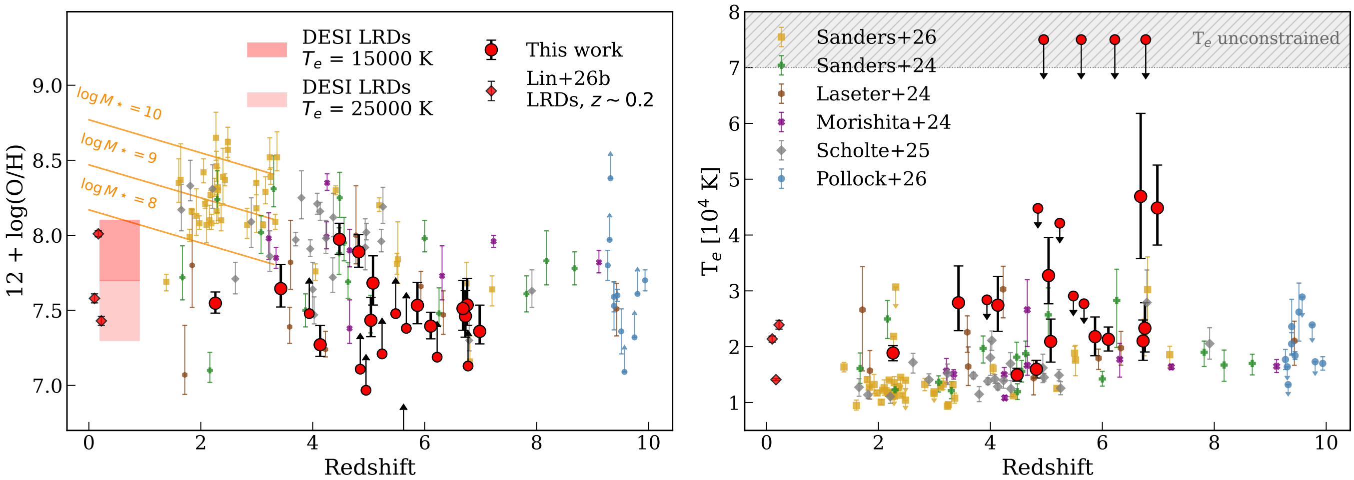

Fig. 5: Metallicities (left) and electron temperatures (right) of our LRD hosts as a function of redshift. Metallicities are inferred from the direct T_e method. The three confirmed low-z LRDs (Lin et al. 2026b) are also shown, as well as shaded regions corresponding to the metallicity distribution of the LRDs in the sample of Lin et al. (2026a) from $0.2 < z < 0.95$ assuming their assumed $T_e = 15\,000$ K (dark pink) and a temperature most consistent with the LRDs in our sample, $T_e = 25\,000$ K (light pink). The high-z star-forming galaxies from Sanders et al. (2024, 2026); Laseter et al. (2024); Morishita et al. (2024); Scholte et al. (2025); Pollock et al. (2026), are also plotted for comparison. The orange solid lines correspond to the Sanders et al. (2021) MZR predictions for $\log M_*/\mathrm{M}_\odot = 8-10$, across the redshift range $0 < z < 3$. The LRD hosts have low metallicities, even compared to hosts at similarly high redshift, and seem to have consistently low metallicity even at quite low redshifts.

metallicity evolution predicted by the mass-metallicity relation (MZR) of Sanders et al. (2021) for a range of stellar-mass bins ($\log M_* = 8-10$) down to $z \sim 0$.

The oxygen abundances and electron temperatures of our sample overlap with those of the general star forming population at the same redshifts: the bulk of the LRDs fall within the locus traced by metal-poor star-forming galaxies, with temperatures in the $T_e \approx 15000-30000$ K range that are characteristic of these systems. In this sense, the narrow components of LRDs are fully compatible with metal-poor star formation. We note, however, a systematic tendency: at a given redshift the LRDs preferentially occupy the lower metallicity/higher temperature edge of the observed distribution, rather than the average.

Interestingly, the deviation of the LRDs from the typical abundance of star-forming galaxies is smallest at $z \sim 7$ and grows steadily as redshift decreases. This deviation becomes most significant for the local LRDs discovered in Lin et al. (2026a,b), which occupy the same part of parameter space as the high-z sample and do not follow the trend of the MZR relation at $z < 2$, visualized in Fig. 5. This has major implications for the evolution of LRDs across cosmic time; if LRD hosts continued to form stars then there would have to be some level of evolution of their metallicity with time. Consequently, either star-formation is completely quenched, or these objects are observed as LRDs at a certain stage of their lifetime. We note that this lack of evolution of the metallicity of LRDs across cosmic time persists even if one adopts $n_e \sim 10^5$ cm^{-3} for our sample.

The agreement between our direct-T_e abundances and the strong-line estimates reported for individual LRDs is also informative. Strong-line calibrations are directly tied to star-formation physics, so their broad consistency with the direct method indicates that the narrow-line component of LRDs is, to first order, governed by metal-poor star formation. At the same time, the highest temperatures we infer ($T_e \gtrsim 3 \times 10^4$ K) are difficult to produce by star formation alone and point to an additional, harder ionising source. This is most evident for rubies-egs61_4233_55604 and rubies-egs63_4233_49140 ($T_e \gtrsim$ 30000 K), which stand out as outliers relative to both the rest of the LRD sample and the $z \sim 7$ comparison galaxies, and may be explained by a contribution from AGN ionisation. A similar argument can be invoked for the LRDs in the sample for which the T_e measurement is unconstrained, due to a low [O III] 4959,5007 Å/[O III] 4363 Å ratio. Taken together, the data hint at a composite scenario in which perhaps both metal-poor star formation and an AGN contribute to the observed line emission on an object-to-object basis. If this is the case, the agreement between the direct and strong-line metallicities further implies that the host galaxy and the AGN narrow-line region of LRDs share similar enrichment properties, i.e. both are likely to be similarly metal-poor.

5.3. Do LRDs deviate from the FMR?

Figure 6 sees our LRD sample placed on the log SFR(Hα)-12+log(O/H) plane, overlaid with the Curti et al. (2024) parameterisation of the Fundamental Metallicity Relation (FMR) at $z = 3-6$ and at $z = 7-10$, evaluated at stellar masses $\log M_*/\mathrm{M}_\odot = 6-10$. All LRD hosts with a direct T_e measurement from Table 1 and a star formation rate (SFR) estimate using the dust-corrected narrow Hα flux (where applicable) are shown. SFRs are computed using the metal-poor conversion factor from Reddy et al. (2022); Shapley et al. (2023).

Our $z < 6$ sources lie mostly around the $z = 3-6$ FMR at stellar masses of $\log M_*/\mathrm{M}_\odot = 7-8.5$, with 4/7 LRD stellar masses consistent with $\log M_*/\mathrm{M}_\odot \sim 7.5$, as well as a lower mass outlier down at $\log M_*/\mathrm{M}_\odot \sim 6$. The higher-redshift ($z \geq 6$) subset is slightly lower in metallicity at fixed SFR, by < 0.5 dex and corresponds to $\log M_*/\mathrm{M}_\odot = 8-9$ in the $z = 7-10$ relation. Given that our median redshift in the lower redshift set is 4.6, but only 6.7 for the higher redshift set, they may be a little closer in inferred

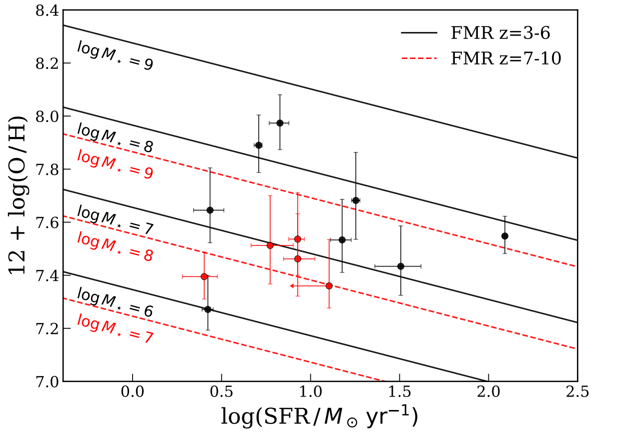

Fig. 6: Metallicities vs. star-formation rate for LRDs with well-constrained metallicities (from the direct-T_e method). We overplot the FMR from Curti et al. (2024) at $z = 3-6$ (black solid lines) and $z = 7-10$ (red dashed lines), for different stellar masses. The FMR-inferred stellar masses for LRD hosts are quite low, $\log M_*/M_\odot \sim 8$.

stellar mass than the above suggests at face value. Regardless, these stellar masses are generally lower than the stellar masses derived in the literature for LRDs, which have mostly relied on SED fitting to what is likely nebular emission from the LRD itself (Sneppen et al. 2026b), and can therefore be treated effectively as upper limits. Estimates vary significantly ($\log M_*/M_\odot = 7-11$), depending on the adopted model (e.g. Leung et al. 2025; Kocevski et al. 2025); although see Juodžbalis et al. (2026) for a dynamical mass upper limit of $\log M_*/M_\odot < 7.3$ for the host galaxy of abell2744-spurs02_9214_41. Assuming that LRD hosts follow the FMR at their respective redshift, their implied stellar masses ($\sim 10^8\,M_\odot$) give very high black hole-to-stellar mass ratios: $M_{BH}/M_* \gtrsim 0.01$, assuming SMBH masses in the range $\log M_{BH} = 6-7$, with ratios larger than unity not ruled out. For example, adopting $\log M_{BH}/M_\odot \sim 6$ for the $\log M_*/M_\odot \sim 6$ outlier, jades-gdn_1181_73488 (Rusakov et al. 2026), gives $M_{BH/M_*} \simeq 1$. This result suggests either that LRDs host SMBHs that, despite their lower masses inferred after correcting for electron-scattering broadening, may still be overmassive with respect to their hosts, or that they deviate from the FMR at their respective redshift. To be consistent with the FMR at a given redshift, would require metallicities 2–3 times what we observe.

Observations at high redshift show a systematic offset from the FMR at $z \sim 0$; by -0.2 dex at $z \sim 3$ down to -0.5 dex at $z \sim 10$, with significant scatter (Pollock et al. 2026). This offset in log(O/H) suggests that for a given metallicity and star formation rate, high-z galaxies are more massive than predicted by the low-z FMR by > 1 dex. That LRDs could be offset from their local FMR has recently been discussed by Isobe et al. (2026) for two LRDs, while Ivey et al. (2026) discuss a possible deviation from the mass-metallicity relation for The Cliff ($z = 3.55$, de Graaff et al. 2025a). As we showed in section 5.2, LRDs are less enriched than other star-forming galaxies at their respective redshifts, hinting that they may indeed systematically deviate from the high-z FMRs, if their stellar masses are not found to be systematically less than inferred from SED fitting analyses. A definitive test would require independent dynamical mass and black hole mass estimates for individual sources.

6. Summary

We have presented the first systematic study of the gas-phase metallicities of Little Red Dots based on medium and high resolution JWST/NIRSpec spectroscopy, providing a catalogue of oxygen abundances for a sample of 24 LRDs at $z \approx 2.3 - 7$, while constraining the electron temperature in 13 objects. We find that:

- Using the direct T_e method applied to the narrow components of observed lines, we recover a sample averaged oxygen abundance of $Z_{T_e} = 0.08^{+0.11}_{-0.03}\,Z_\odot$ with an average electron temperature of $T_e = 23000^{+17000}_{-7000}$. LRD hosts are therefore metal-poor, but not chemically pristine.
- The $\hat{R}$ strong line calibration yields a fully consistent sample average of $Z_{\hat{R}} = 0.07^{+0.07}_{-0.04}\,Z_\odot$, with the 1σ T_e-to-$\hat{R}$ metallicity scatter being just 4% in 12+log(O/H) space. The $\hat{R}$ calibration can thus be used to safely constrain the oxygen abundances of LRD hosts. Combining the direct T_e and N2-based upper limits on metallicity yields a joint average of $Z_{joint} = 0.08^{+0.09}_{-0.04}\,Z_\odot$.
- We find two very metal poor LRDs in the sample, abell2744-spurs02_9214_41 (A2744-QSO1 $z \sim 7.04$), with $Z < 1.3\%\,Z_\odot$, and jades-gds-w09_1212_2993 ($z \sim 4.88$), with $Z = 0.3\%\,Z_\odot$, constrained using the $\hat{R}$ calibration. These are the only two objects in the sample that approach the abundances theoretically required for DCBH-based formation.
- Comparing grating and PRISM derived abundances, we find large object-to-object scatter of up to ~ 0.8 dex at 1σ. PRISM spectra at the usual redshift range of LRDs, lack the resolution to sufficiently decompose the Hβ +[O III] 4959,5007 Å, and Hγ +[O III] 4363 Å complexes, and PRISM-based direct T_e metallicities of samples of LRDs should be treated with caution.
- The metallicities and temperatures of LRDs are within the range of the general metal-poor star forming population at the same redshifts, but preferentially occupy the lower-metallicity/higher-temperature edge of the distribution.
- LRD metal abundances remain remarkably constant across cosmic time, suggesting that low metallicity is a defining characteristic of LRDs.
- Placing LRDs on the FMR implies low stellar masses, $\log M_*/M_\odot \sim 7-9$. The average black hole masses quoted for LRDs in the literature either imply that they host SMBHs that are overmassive for their hosts, or that they deviate from the FMR at their respective redshifts.

Taken together, our results indicate that the narrow line emission in LRDs is largely consistent with a metal-poor star-forming host, though a subset shows signatures of an additional harder ionising source. In a scenario where the narrow emission is a composite of a host galaxy and an AGN, our results imply that the enrichment of the two components is similar. Probing the chemical enrichment of the cocoon around the central engine is an important future endeavour to discriminate for certain that the LRD and its host share the same metal abundance. This might be done with oxygen or iron permitted lines with a suitable modelling of the Lyβ radiative transfer or with observations of semi-forbidden lines with high critical density, possibly in the rest-frame UV. Finally, to truly paint a coherent picture of the nature of LRDs and establish their relation to the FMR and their black hole to host galaxy mass ratio, will require independent dynamical and black-hole mass estimates for several individual sources (e.g. Juodžbalis et al. 2026).

Data availability

This paper makes use of public JWST data downloaded from the DAWN JWST Archive (DJA)[1].

Acknowledgements. The Cosmic Dawn Center (DAWN) is funded by the Danish National Research Foundation under grant DNRF140. The data products presented herein were retrieved from the DAWN JWST Archive (DJA). DJA is an initiative of the Cosmic Dawn Center. DW, GPN and AS are co-funded by the European Union (ERC, HEAVYMETAL, 101071865). Views and opinions expressed are, however, those of the authors only and do not necessarily reflect those of the European Union or the European Research Council. Neither the European Union nor the granting authority can be held responsible for them. KEH acknowledges funding from the Swiss State Secretariat for Education, Research and Innovation (SERI). This work is based in part on observations made with the NASA/ESA/CSA James Webb Space Telescope. The data were obtained from the Mikulski Archive for Space Telescopes (MAST) at the Space Telescope Science Institute, which is operated by the Association of Universities for Research in Astronomy, Inc., under NASA contract NAS 5-03127 for JWST. These observations are associated with programmes #1180, #1181, #1286, #1212, #9223, #3567, #4233, #1345, #4106, #4287 and #9214.

References

Akins H. B., et al., 2024, arXiv e-prints, p. arXiv:2406.10341
Arellano-Córdova K. Z., et al., 2026, MNRAS, 547, stag380
Asplund M., Grevesse N., Sauval A. J., Scott P., 2009, ARA&A, 47, 481
Atek H., et al., 2025, arXiv e-prints, p. arXiv:2511.07542
Baggen J. F. W., Scoggins M. T., van Dokkum P., Haiman Z., Torralba A., Matthee J., 2026, ApJ, 1002, L4
Barro G., et al., 2025, arXiv e-prints, p. arXiv:2512.15853
Baskin A., Laor A., 2005, MNRAS, 358, 1043
Begelman M. C., Dexter J., 2025, arXiv e-prints, p. arXiv:2507.09085
Bellovary J., 2025, arXiv e-prints, p. arXiv:2501.03309
Binggeli C., et al., 2019, MNRAS, 489, 3827
Brammer G., 2023, msaexp: NIRSpec analyis tools, https://doi.org/10.5281/zenodo.8319596, doi:10.5281/zenodo.8319596, https://doi.org/10.5281/zenodo.8319596
Brazzini M., et al., 2026, arXiv e-prints, p. arXiv:2601.22214
Brooks M., et al., 2025, ApJ, 986, 177
Bunker A. J., et al., 2024, A&A, 690, A288
Cameron A. J., Katz H., Rey M. P., Saxena A., 2023, MNRAS, 523, 3516
Cameron A. J., et al., 2026, arXiv e-prints, p. arXiv:2601.15964
Cataldi E., et al., 2025, arXiv e-prints, p. arXiv:2512.07955
Cenci E., Habouzit M., 2025, MNRAS, 542, 2597
Chakraborty P., et al., 2025, ApJ, 985, 24
Chang S.-J., Gronke M., Matthee J., Mason C., 2026, MNRAS, 545, staf2131
Chen Z., et al., 2026, arXiv e-prints, p. arXiv:2604.21516
Comastri A., et al., 2026, A&A, 706, A302
Curti M., et al., 2024, A&A, 684, A75
D'Eugenio F., et al., 2025a, arXiv e-prints, p. arXiv:2510.00101
D'Eugenio F., et al., 2025b, arXiv e-prints, p. arXiv:2510.00101
D'Eugenio F., et al., 2026, MNRAS, 545, staf2117
Davis K., et al., 2026, arXiv e-prints, p. arXiv:2606.00258
Eisenstein D. J., et al., 2026, ApJS, 283, 6
Feroz F., Hobson M. P., Bridges M., 2009, MNRAS, 398, 1601
Finkelstein S. L., et al., 2023, ApJ, 946, L13
Gordon K. D., 2024, Journal of Open Source Software, 9, 7023
Gordon K. D., et al., 2024, ApJ, 970, 51
Greene J. E., et al., 2024, ApJ, 964, 39
Harikane Y., et al., 2023, ApJ, 959, 39
Heintz K. E., et al., 2025, A&A, 693, A60
Inayoshi K., Maiolino R., 2025, ApJ, 980, L27
Inayoshi K., Murase K., Kashiyama K., 2025, arXiv e-prints, p. arXiv:2509.19422
Isobe Y., et al., 2023, ApJ, 959, 100
Isobe Y., et al., 2026, arXiv e-prints, p. arXiv:2606.11345
Ito K., et al., 2025, arXiv e-prints, p. arXiv:2506.22642
Ivey L. R., et al., 2026, arXiv e-prints, p. arXiv:2604.09177
Jakobsen P., et al., 2022, A&A, 661, A80
Ji X., et al., 2026, MNRAS, 545, staf2235
Juodžbalis I., et al., 2024, MNRAS, 535, 853
Juodžbalis I., et al., 2025, arXiv e-prints, p. arXiv:2504.03551
Juodžbalis I., et al., 2026, Nature, 653, 1017
Kido D., Ioka K., Hotokezaka K., Inayoshi K., Irwin C. M., 2025, MNRAS, 544, 3407
Killi M., et al., 2024, A&A, 691, A52
Kocevski D. D., et al., 2024, arXiv e-prints, p. arXiv:2404.03576
Kocevski D. D., et al., 2025, ApJ, 986, 126
Kokorev V., et al., 2025, arXiv e-prints, p. arXiv:2511.07515
Koposov S., et al., 2024, joshspeagle/dynesty: v2.1.4, doi:10.5281/zenodo.12537467, https://doi.org/10.5281/zenodo.12537467
Laseter I. H., et al., 2024, A&A, 681, A70
Leung G. C. K., et al., 2025, ApJ, 992, 26
Lin X., et al., 2026a, arXiv e-prints, p. arXiv:2605.21574
Lin X., et al., 2026b, ApJ, 997, 364
Luridiana V., Morisset C., Shaw R. A., 2015, A&A, 573, A42
Maiolino R., et al., 2024, Nature, 627, 59
Maiolino R., et al., 2025a, arXiv e-prints, p. arXiv:2505.22567
Maiolino R., et al., 2025b, Monthly Notices of the Royal Astronomical Society, 538, 1921
Martins F., Schaerer D., Marques-Chaves R., et al., 2026, arXiv e-prints, p. arXiv:2605.12141
Maseda M. V., et al., 2024, A&A, 689, A73
Mason C., et al., 2023, Deep Spectroscopy of the First Ionized Bubbles: New Insight into the Beginning of Reionization, JWST Proposal. Cycle 2, ID. #4287
Matthee J., et al., 2024, ApJ, 963, 129
Matthee J., et al., 2026, arXiv e-prints, p. arXiv:2603.17667
Morales-Luis A. B., Pérez-Montero E., Sánchez Almeida J., Muñoz-Tuñón C., 2014, ApJ, 797, 81
Morishita T., et al., 2024, ApJ, 971, 43
Morisset C., Luridiana V., García-Rojas J., Gómez-Llanos V., Bautista M., Mendoza C., 2020, Atoms, 8
Naidu R. P., et al., 2025, arXiv e-prints, p. arXiv:2503.16596
Nandal D., Loeb A., 2025, arXiv e-prints, p. arXiv:2507.12618
Nelson E., et al., 2023, Extremely massive galaxies in the early universe: a challenge to Lambda-CDM?, JWST Proposal. Cycle 2, ID. #4106
Nikopoulos G. P., Watson D., Sneppen A., Rusakov V., Heintz K. E., Witstok J., Brammer G., 2026, A&A, 710, A136
Nishigaki M., et al., 2025, arXiv e-prints, p. arXiv:2512.12983
Omukai K., Schneider R., Haiman Z., 2008, ApJ, 686, 801
Osterbrock D. E., Ferland G. J., 2006, Astrophysics of gaseous nebulae and active galactic nuclei
Pacucci F., Ferrara A., Kocevski D. D., 2026, arXiv e-prints, p. arXiv:2601.14368
Park K., Torralba A., Matthee J., Mascia S., Haiman Z., Naidu R. P., de Graaff A., 2026, arXiv e-prints, p. arXiv:2605.14233
Pérez-González P. G., et al., 2026, arXiv e-prints, p. arXiv:2602.20247
Pollock C. L., et al., 2026, A&A, 708, A203
Reddy N. A., et al., 2022, ApJ, 926, 31
Rusakov V., et al., 2026, Nature, 649, 574
Sanders R. L., et al., 2021, ApJ, 914, 19
Sanders R. L., Shapley A. E., Topping M. W., Reddy N. A., Brammer G. B., 2024, ApJ, 962, 24
Sanders R. L., et al., 2026, ApJ, 1003, 228
Scholte D., et al., 2025, MNRAS, 540, 1800
Setton D. J., et al., 2025, ApJ, 995, 118
Shapley A. E., Sanders R. L., Reddy N. A., Topping M. W., Brammer G. B., 2023, ApJ, 954, 157
Skilling J., 2004, in Fischer R., Preuss R., Toussaint U. V., eds, American Institute of Physics Conference Series Vol. 735, Bayesian Inference and Maximum Entropy Methods in Science and Engineering: 24th International Workshop on Bayesian Inference and Maximum Entropy Methods in Science and Engineering. AIP, pp 395–405, doi:10.1063/1.1835238
Skilling J., 2006, Bayesian Analysis, 1, 833
Sneppen A., et al., 2026a, arXiv e-prints, p. arXiv:2601.18864
Sneppen A., et al., 2026b, arXiv e-prints, p. arXiv:2604.09399
Sneppen A., Watson D., Matthews J. H., Sim S. A., 2026c, arXiv e-prints, p. arXiv:2605.15263
Speagle J. S., 2020, MNRAS, 493, 3132
Tang M., et al., 2025, ApJ, 991, 217
Tang M., et al., 2026, arXiv e-prints, p. arXiv:2604.03563
Torralba A., et al., 2026, A&A, 707, A75
Tortosa A., Ricci C., Du P., Venturi G., Ho L. C., Li R., Wang J.-M., Berton M., 2026, A&A, 708, A293
Tripodi R., et al., 2024, arXiv e-prints, p. arXiv:2412.04983
Wang B., et al., 2026, arXiv e-prints, p. arXiv:2602.06024
Whitler L., Stark D. P., Mason C. A., Tang M., Chen Z., Lu T.-Y., Prieto-Lyon G., Hutter A., 2026, MNRAS, 548, stag639
Yan Z., Inayoshi K., Chen K., Guo J., 2025, arXiv e-prints, p. arXiv:2512.11050
Zhang Y., Morishita T., Stiavelli M., 2026a, ApJ, 998, 141
Zhang Z., Jiang L., Liu W., Ho L. C., Inayoshi K., 2026b, ApJ, 998, 170
de Graaff A., et al., 2024, A&A, 684, A87
de Graaff A., et al., 2025a, arXiv e-prints, p. arXiv:2503.16600
de Graaff A., et al., 2025b, arXiv e-prints, p. arXiv:2511.21820
de Graaff A., et al., 2025c, A&A, 697, A189
de Graaff A., et al., 2025d, A&A, 697, A189
de Graaff A., et al., 2025e, A&A, 701, A168

[1] DOI: 10.5281/zenodo.8319596

Appendix A: Flux measurements

Table A.1: Narrow line fluxes for the LRD sample

ID	Object	z	F([O III] D)	F([O III])	F([O II])	F([Ne III])	F([N II])	F(Hα)	F(Hβ)
1	abell2744-spurs02_9214_41	7.037	< 5	< 2	< 3	< 3	< 4	< 72	3^{+1}_{-1}
2	rubies-egs61_4233_55604	6.983	147^{+2}_{-2}	9^{+1}_{-1}	< 10	14^{+2}_{-2}	< 3	< 62	14^{+3}_{-5}
3	rubies-uds42_4233_807469	6.775	72^{+2}_{-2}	< 7	< 8	4^{+1}_{-1}	< 3	< 30	9^{+2}_{-2}
4	jades-gdn2_1181_954	6.760	150^{+3}_{-3}	5^{+1}_{-1}	< 7	7^{+1}_{-1}	< 3	36^{+3}_{-4}	14^{+2}_{-2}
5	egs-nelsonx_4106_47962	6.728	150^{+2}_{-2}	4^{+1}_{-1}	< 13	7^{+2}_{-1}	< 4	37^{+9}_{-6}	21^{+2}_{-2}
6	rubies-egs63_4233_49140	6.685	143^{+2}_{-2}	7^{+2}_{-2}	6^{+2}_{-2}	12^{+2}_{-2}	< 2	26^{+9}_{-6}	12^{+3}_{-3}
7	glimpse-obs01b_9223_5536	6.223	$11.0^{+0.4}_{-0.4}$	< 1	—	—	< 2	< 6	$1.1^{+0.4}_{-0.4}$
8	glimpse-obs01_9223_12248	6.108	65^{+1}_{-1}	$1.8^{+0.3}_{-0.3}$	—	—	< 1	14^{+3}_{-3}	$9.6^{+0.4}_{-0.4}$
9	jades-gdn_1181_38147	5.869	259^{+3}_{-3}	7^{+2}_{-2}	16^{+3}_{-3}	9^{+2}_{-2}	< 9	89^{+11}_{-12}	28^{+2}_{-2}
10	rubies-uds3_4233_47509	5.672	199^{+3}_{-3}	< 9	—	—	< 3	73^{+9}_{-20}	20^{+3}_{-3}
11	ceers_1345_746	5.622	22^{+1}_{-1}	< 9	< 5	< 5	< 3	8^{+3}_{-2}	< 5
12	jades-gds05_1286_204851	5.482	138^{+2}_{-2}	< 7	7^{+2}_{-2}	7^{+2}_{-1}	< 1	24^{+5}_{-5}	12^{+2}_{-2}
13	ceers-egs_1345_2782	5.239	96^{+2}_{-2}	< 6	< 7	5^{+1}_{-1}	< 2	< 45	10^{+3}_{-3}
14	jades-gds06_1286_159717	5.077	552^{+6}_{-6}	15^{+4}_{-4}	56^{+9}_{-9}	32^{+6}_{-6}	< 7	149^{+8}_{-8}	48^{+5}_{-5}
15	jades-gdn_1181_68797	5.039	370^{+22}_{-26}	17^{+3}_{-3}	59^{+6}_{-6}	30^{+3}_{-3}	< 30	272^{+81}_{-77}	37^{+7}_{-10}
16	valentino-egs_3567_42232	4.952	25^{+1}_{-1}	< 4	< 6	3^{+1}_{-1}	< 2	26^{+6}_{-7}	4^{+1}_{-1}
17	jades-gdn_1181_39353	4.849	58^{+2}_{-2}	< 4	< 7	< 8	< 2	32^{+4}_{-7}	9^{+2}_{-2}
18	jades-gds-w09_1212_2993[1]	4.824	9^{+2}_{-2}	< 17	< 10	7^{+2}_{-2}	< 18	91^{+6}_{-6}	19^{+2}_{-2}
19	jades-gds02_1286_38562	4.821	196^{+2}_{-2}	3^{+1}_{-1}	10^{+1}_{-1}	10^{+1}_{-1}	< 2	48^{+2}_{-3}	18^{+1}_{-1}
20	ceers-egs_1345_1244	4.477	494^{+19}_{-18}	7^{+1}_{-1}	23^{+3}_{-3}	21^{+2}_{-2}	5^{+2}_{-2}	75^{+9}_{-10}	44^{+6}_{-5}
21	jades-gdn_1181_73488	4.133	152^{+1}_{-1}	6^{+1}_{-1}	< 7	7^{+1}_{-1}	< 3	36^{+3}_{-3}	22^{+1}_{-1}
22	jades-gds-wide_1180_13329	3.938	190^{+3}_{-3}	< 9	20^{+5}_{-5}	11^{+3}_{-3}	< 7	63^{+5}_{-7}	16^{+3}_{-2}
23	jades-gdn_1181_53501	3.429	282^{+4}_{-4}	11^{+3}_{-2}	< 22	< 24	< 3	57^{+11}_{-11}	18^{+4}_{-4}
24	jades-gdn2_1181_28074	2.260	15449^{+194}_{-214}	352^{+42}_{-45}	2747^{+61}_{-61}	2014^{+39}_{-38}	87^{+22}_{-23}	7080^{+174}_{-175}	2392^{+111}_{-107}

Notes. All fluxes are given in units of 10^{-19} ergs s^{-1} cm^{-2}, and have been corrected for dust where applicable. F([O III] D) denotes the flux in the [O III] 4959,5007 Å doublet, F([O III]) corresponds to the flux in the [O III] 4363 Å line, while F([O II]), F([Ne III]), and F([N II]) correspond to the fluxes in the [O II] 3726,3729 Å doublet, [Ne III] 3869 Å, and [N II] 6583 Å lines respectively.
(1) The [O III] 4959,5007 Å, [O II] 3726,3729 Å, [Ne III] 3869 Å and Hβ fluxes quoted for this object are estimated using PRISM spectra.